Impact of spherical projectiles into a viscoplastic fluid

Hervé Tabuteau,[1,2] Darek Sikorski,[1,3] Simon J. de Vet,[1,4] and John R. de Bruyn[1,*]
[1]*Department of Physics and Astronomy, University of Western Ontario, London, Ontario, Canada N6A 3K7*
[2]*Université Rennes 1, IPR, CNRS, UMR 6251, Campus Beaulieu, F-35042 Rennes, France*
[3]*Department of Biomedical Engineering, University of British Columbia, Vancouver, British Columbia, Canada V6T 1Z1*
[4]*Department of Physics and Atmospheric Science, Dalhousie University, Halifax, Nova Scotia, Canada B3H 3J5*
(Received 6 January 2011; revised manuscript received 12 May 2011; published 16 September 2011)

We study the behavior of a yield-stress fluid following the impact of a vertically falling sphere. Since the impact produces shear stresses larger than the yield stress, the material in the vicinity of the impact becomes fluidized. The sphere entrains air when it enters the fluid, and the resulting cavity pinches off below the surface. The upper part of this cavity then rebounds upward. For sufficiently fast impacts, a vertical jet is produced by the cavity collapse. While many aspects of this process are similar to that in Newtonian fluids or granular materials, the rheological properties of our target material change the scaling of the cavity pinch-off depth and have a dramatic effect on the height of the jets. The material returns to a solid-like behavior once the stresses due to the impact have relaxed to below the yield stress, leaving a crater in the surface of the material. We find that the diameter of this crater depends nonmonotonically on the impact speed. The crater shape also changes with speed, reflecting the dynamics of the impact process.

DOI: 10.1103/PhysRevE.84.031403 PACS number(s): 82.70.−y, 83.60.La, 83.80.Kn

I. INTRODUCTION

The impact of a solid projectile onto a target is a subject of longstanding interest and importance. On the planetary scale, the formation of impact craters is one of the most important processes involved in the evolution of planetary surfaces [1]. On a smaller scale, the impact of solid or fluid projectiles into fluid targets [2–11] or granular materials [12–25] is an everyday occurrence which plays a role in many applications. From a fundamental perspective, the dynamics of the impact process is complex, and several aspects remain incompletely understood.

Recently there has been substantial interest in studying low-energy impacts in granular materials [14–25]. Some of this work has been motivated by the expectation that the rheological properties of a granular material will be similar to those of the rock debris or melt produced in a large-scale impact. In particular, the granular material will not flow unless sufficient energy is injected into it (i.e., by the impact). It will then flow until the injected energy is dissipated by friction or inelastic collisions among the grains, at which time it will return to its solid-like quiescent state. Although the energy scale of laboratory granular impact experiments is many orders of magnitude smaller than that of planetary impacts, several features of the impact dynamics, the morphology of the resulting craters, and the energy scaling of the crater dimensions resemble those of planetary craters [15,16]. There are also, as might be expected, some significant differences [25]. Impacts and the resulting penetration of the projectile into the granular target have also been used as a probe of the drag force, and of force transmission in granular materials in general [18,22–24].

The subsurface flows following an impact have been studied in transparent fluids [2,3,8,26–28] and in granular materials in quasi-two-dimensional geometries [16] or through the use of x-ray photography [20]. Many aspects of the subsurface dynamics are similar in the two cases. Specifically, the projectile entrains air as it enters the target material, forming a cavity extending from the surface of the projectile up to the free surface of the target. Hydrostatic pressure in the fluid acts to force the cavity walls radially inward, resisted by viscous forces and inertia [16]. The result is that the cavity radius will shrink fastest and pinch off at a particular depth. The pinch-off dynamics, and in particular the time dependence of the diameter of the neck at the pinch-off point, has been studied both experimentally [2,3,8,16,20,26–28,56] and theoretically [5,54,55]. In both the fluid and granular cases the increase in pressure due to the cavity pinch-off produces jets directed both upward and downward [13,16,20,27,29]. The upward jets can rise to very substantial heights [2]. It was shown in Refs. [6,7] that fluid elasticity causes a significant decrease in the jet height.

In the early 1980s, high-velocity impacts into clay-water or clay-oil mixtures were investigated as a model for planetary crater formation [30–33]. These materials are viscoplastic; that is, they have a yield stress τ_c and behave as elastic solids when subjected to a shear stress less than τ_c but flow when the stress is larger than τ_c. The viscoplastic rheology mimics that of rock debris following an impact, and in particular it was suggested that the presence of a yield stress could explain aspects of planetary impact crater morphology [30,32].

In this paper we study the impact of solid spheres falling vertically into a transparent viscoplastic gel. Our goals are to investigate the links between the crater formation process and the subsurface dynamics resulting from the impact in a yield stress fluid with reasonably well-known and controllable material properties, to compare our results with those from impacts into Newtonian fluids and granular materials, and to investigate the extent to which low-velocity impacts into yield-stress fluids can be used as a model for geophysical impacts. The target material is Carbopol, a commercial rheology modifier based on cross-linked poly(acrylic acid)

*debruyn@uwo.ca

 ©2011 American Physical Society

chains [34]. Aqueous dispersions of Carbopol have a yield stress that depends on both Carbopol concentration and pH [35,36]. Our targets are thus initially soft solids, but the impact of a sufficiently energetic projectile induces stresses sufficient to overcome the yield stress in a region surrounding the projectile, causing the target material in this region to flow. As the shear stress in the material decreases after the impact, however, it reverts to a solid state and any deformation of the target's surface becomes "frozen in." Because Carbopol is transparent, we are able to study the subsurface dynamics at all stages of the impact process. Here we present results on the size and shape of the craters formed by the impact, the pinch-off of the entrained subsurface air cavity, and the behavior of the jets that form when the cavity collapses.

II. EXPERIMENT AND RHEOLOGICAL CHARACTERIZATION

We studied the impact of spheres into dispersions of Carbopol ETD 2050 at concentrations varying from 0.3% to 2.2% by weight. When mixed with water and pH-neutralized, Carbopol forms stable, highly transparent viscoplastic gels which display minimal thixotropy. Our samples were prepared by slowly adding the required amount of Carbopol powder with continuous stirring to deionized water. Sodium hydroxide solution was then added to raise the pH to 6. The suspension was then homogenized and bubbles removed by several days of vigorous mixing [37].

The rheological properties of the Carbopol gels were measured with an Ares RHS controlled-strain rheometer. The storage and loss moduli G' and G'' were measured as a function of frequency by applying small-amplitude oscillatory strains. In all cases $G' \gg G''$ and G' was relatively independent of frequency, as observed previously [35,36,38,39]. The yield stress was obtained by fitting data for the steady-state shear stress τ as a function of shear rate $\dot{\gamma}$ to the Herschel-Bulkley model,

$$\tau = \tau_c + K\dot{\gamma}^n, \tag{1}$$

with τ_c, the consistency K, and the power-law index n treated as fitting parameters. In all cases this form described the data well, as has been found previously [38–40]. The values of τ_c, K, and n for the dispersions used in this work are summarized in Table I, along with the low-frequency limit of the storage modulus, which we refer to as the elastic modulus G. All measurements were performed at room temperature.

The Carbopol was poured into a container 12.7 cm square in cross section and 25 cm deep. The container was overfilled and stirred, then a straight edge was used to remove excess Carbopol and make the free surface flat. Although surface waves caused by the impacts can reach the walls of this container, we verified by experiments on smaller containers that the dimensions of the craters formed in our experiments did not depend on container size. Experiments were performed by dropping spheres of diameter d_b and density ρ_b from a holder positioned a height h above the free surface of the container of Carbopol. Spheres of a variety of materials and sizes were used, as summarized in Table II. The release height h, measured from the bottom of the sphere to the Carbopol surface, ranged from 0.002 to 1.8 m. The trajectory of the sphere as it fell through the transparent fluid was recorded using a high-speed video camera (Motionscope, Redlake Imaging) with a typical frame rate of 250 frames per second. Video images were later analyzed to obtain the depth z of the sphere as a function of time, as well as the shape and dimensions of the entrained air cavity produced during the impact. Here z is measured from the level of the original Carbopol surface to the bottom of the sphere. Between runs the Carbopol was stirred to remove any bubbles left behind from the previous run. Additional Carbopol was then added as necessary and the surface re-smoothed. Experiments on a given material were typically performed over a period of a few days, and the Carbopol was covered when not in use to minimize evaporation.

TABLE I. Rheological properties of the Carbopol dispersions used in the experiments.

Conc. (wt %)	τ_c (Pa)	K (Pa s^n)	n	G (Pa)
0.3	7.5 ± 0.4	6.6 ± 0.4	0.46 ± 0.1	39
0.5	9.3 ± 0.6	6.7 ± 0.5	0.49 ± 0.01	44.5
0.8	17.0 ± 1.0	9.7 ± 0.8	0.51 ± 0.02	75
1.0	25.0 ± 0.9	12.0 ± 0.5	0.54 ± 0.01	91
1.2	29.8 ± 1.4	11.6 ± 1.1	0.55 ± 0.02	120
2.2	45.2 ± 1.7	10.2 ± 1.2	0.60 ± 0.02	170

TABLE II. Properties of the spheres used as projectiles.

Material	Diameter d_b (m)	Density ρ_b (kg/m^3)
acetal	0.0254	1340
aluminum oxide	0.0127	3690
steel	0.0127	7790
steel	0.0191	7790
stainless steel	0.0254	7890
bronze	0.0191	8810
tungsten carbide	0.0127	14970

The diameter of the impact crater was determined by averaging three measurements, made with a set of calipers, of the distance from crest to crest of the raised rim surrounding the crater. The depth of the crater was typically small (on the order of 1 mm) and difficult to measure accurately, but in a few cases we measured the full three-dimensional profile of the crater using a scanning laser profilometer that is described in detail in Ref. [25]. A low-power HeNe laser beam is passed through a cylindrical lens to form a laser sheet, which is directed onto the Carbopol surface at an angle from the vertical. Variations in the height of the material surface cause the laser line to appear curved when imaged from above with a CCD camera, and the vertical coordinate of the crater surface can be calculated from the horizontal deflections of the line [25]. Because the Carbopol is transparent, we found it necessary to sprinkle some small spherical glass beads on its surface to make the laser line visible. Profiles were measured on runs performed using a container 25 cm square by 25 cm deep.

Several dimensionless numbers can be introduced to characterize the dynamics of the impact and the resulting flow.

Planetary impacts are typically characterized by the inverse Froude number [1],

$$\mathrm{Fr}^{-1} = g d_b / 2 v_i^2, \tag{2}$$

where v_i is the impact velocity and g the acceleration due to gravity. Fr^{-1} at impact ranges from 0.0035 to 6.35 in our experiments. For comparison, $10^{-6} \lesssim \mathrm{Fr}^{-1} \lesssim 10^{-2}$ for planetary impacts [1], and $0.002 \leqslant \mathrm{Fr}^{-1} \leqslant 0.32$ for the granular impact experiments of Refs. [15,25]. The Reynolds number is

$$\mathrm{Re} = \rho_f v_i d_b / \eta \sim \rho_f v_i^{2-n} d_b^n / K, \tag{3}$$

where ρ_f is the fluid density. Here the shear rate is approximated by $\dot{\gamma} \sim v_i / d_b$ and the viscosity $\eta = \tau / \dot{\gamma}$ is determined from Eq. (1). Re is in the range $0.7 \leqslant \mathrm{Re} \leqslant 440$ at impact, so inertia dominates initially, except for very low release heights. Estimating the surface tension γ of Carbopol to be 0.034 J/m^2 [41], we find the Weber number

$$\mathrm{Wb} = \rho_f v_i^2 d_b / \gamma \tag{4}$$

to be in the range $15 \leqslant \mathrm{Wb} \leqslant 2.7 \times 10^4$ for our experiments, so the effects of surface tension are always negligible. The Bingham number Bi, which indicates the relative importance of the yield stress to viscous effects, is defined as

$$\mathrm{Bi} = \tau_c d_b^n / K v_i^n. \tag{5}$$

Bi ranges from 0.07 to 1.29 in our work, suggesting that yield stress effects are small immediately following the impact in most of our runs. Finally, the Mach number Ma, which is the ratio of the impact speed to the speed c of shear waves in the Carbopol [42], is given by

$$\mathrm{Ma} = v_i / c = v_i \rho_f^{1/2} / G^{1/2}, \tag{6}$$

where G is the elastic modulus of the fluid. Ma ranges from 0.48 to 28.2 in our experiments, indicating that most of our impacts are supersonic [42].

III. RESULTS

A. Phenomenology

The sequence of events following the impact of a 1.27 cm diameter aluminum oxide sphere dropped from a height $h = 0.440$ m into a 0.5% Carbopol gel is shown in Fig. 1. In this experiment, the sphere hits the fluid surface with an impact velocity $v_i = (2gh)^{1/2} = 2.94$ m/s, giving an initial Reynolds number of 89 (Ma = 14). As it penetrates the material, it generates a splash [2] and a rapidly damped surface wave. The sphere entrains air as it moves downward, forming a cavity of radius $r(z)$ which extends from the sphere up to the free surface, as illustrated in Fig. 1(a). The cavity becomes further drawn out as the sphere continues to sink through the gel. It starts to collapse inward, as seen in Fig. 1(b), and eventually pinches off [i.e., $r(z)$ becomes equal to zero] at a particular depth z_v and time t_v [Fig. 1(c)]. The upper portion of air cavity then retracts upward toward the Carbopol surface, as in Fig. 1(d). For sufficiently high impact velocities, a jet is formed as a result of inertial focusing when the inward-moving cavity wall reaches $r = 0$. This jet then shoots upward above the fluid surface, as seen in Figs. 1(e) and 1(f). The Carbopol in the region of the impact flows until the internal stress becomes smaller than the yield stress, at which point the material becomes solid and flow ceases. The crater which remains in the surface of the Carbopol is thus a result of the combined effects of the flow and surface waves generated by the impact, the retraction and filling in of the upper portion of the pinched-off air cavity, and the process that produces the jet.

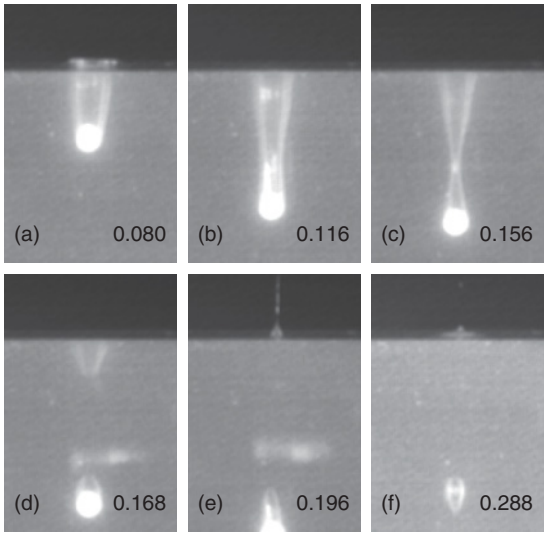

FIG. 1. The penetration of an aluminum oxide sphere with $d_b = 1.27$ cm and $h = 0.440$ m into a 0.5% Carbopol dispersion. The time in seconds after the initial impact of the sphere with the surface is indicated at the bottom left corner of each image. The sequence of events is discussed in the text. The pinch-off of the entrained air cavity, which occurs at $t = 0.156$ s, results in the formation of a vertical jet which can be seen in the last two images.

A crater formed by an impact with a relatively high initial Reynolds number, Re = 138 (Ma = 15), is shown in Fig. 2. Figure 2(a) is a three-dimensional image of the crater measured with the laser profilometer described above. Figure 2(b) is a contour map of the same crater, and Fig. 2(c) shows the azimuthally averaged depth profile of the crater as a function of distance from the crater's center. The crater is much wider than it is deep (note the different vertical and horizontal scales in Fig. 2), with a fairly broad interior region, a pronounced central peak which is the remnant of the jet formation described above, and a well-defined circular rim that is relatively high compared to the crater's depth. The mean surface level in Fig. 2(c) is higher than the original level of zero due to the volume of the entrained air bubbles that remain trapped in the Carbopol.

At lower impact velocities, the volume of air entrained by the falling sphere is smaller, and the cavity pinch-off occurs much closer to the surface. In such cases, the pinch-off is not energetic enough to produce an observable jet. The upper portion of the cavity simply relaxes toward the surface, eventually reaching its final shape when the stress drops below τ_c. A crater formed in this lower speed regime is shown in Fig. 3; here the Reynolds number at impact was 24 (Ma = 4.7). The crater is roughly conical, although the interior surfaces are slightly convex, and has a low, somewhat irregular rim. A very small central peak can be seen in Fig. 3, suggesting that in this

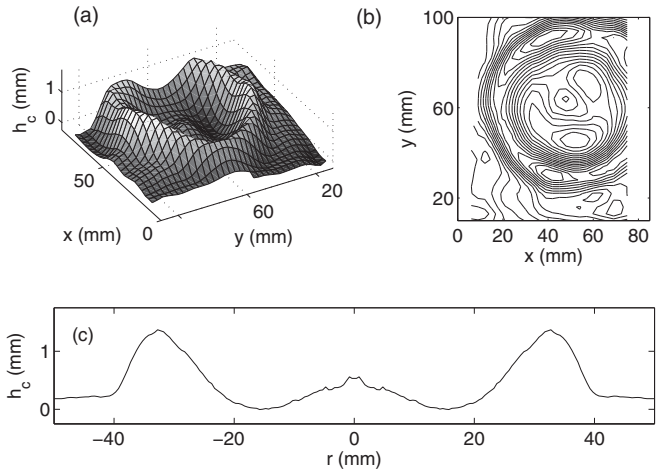

FIG. 2. (a) The three-dimensional surface of a crater formed in a relatively high speed impact. Here $c = 0.5$ wt %, and a 2.54 cm stainless steel sphere was dropped from $h = 0.50$ m, giving Re = 138. The crater has a well-defined circular rim, a relatively small depth, and a strong central peak. (b) shows a contour plot of the same crater. (c) The azimuthally averaged crater profile. Note the different scales on the vertical and horizontal axes.

particular experiment the pinch-off of the air cavity produced a very small amount of upward momentum, but not enough to generate a fully formed jet. For impact conditions intermediate between those of Figs. 2 and 3, the craters have the flatter interior and more pronounced central peak of the higher speed crater shown in Fig. 2, but without the well-defined raised rim.

For all impact conditions, the lower portion of the entrained air cavity remains attached to the top of the sinking sphere after the cavity pinches off. If its volume is sufficiently large, it can itself pinch off, leading to the formation of one or a series of bubbles. If these bubbles are large enough that their buoyancy overcomes the yield stress, they can rise through the Carbopol [49] and, if they reach the surface, will affect the shape of the crater in a difficult-to-control manner. Ultimately, whatever air remains attached to the top of the sphere takes the shape of an approximately conical cap. The sphere continues to sink, its downward speed eventually reaching a terminal value (which may be zero) that depends on the density and size of the sphere as well as the properties of the fluid [37]. Under some conditions, the falling sphere undergoes damped oscillations due to the elasticity of the Carbopol [42,43] before reaching its terminal speed. In these cases, the pinch-off of the air cavity takes place before the sphere's first oscillation.

B. Crater dimensions and scaling

Figure 4 shows the diameter d_c of craters formed in four typical sets of experiments, each involving a different combination of projectile and Carbopol target, plotted as a function of the release height h of the sphere. The dependence of d_c on h appears to be complex and rather different in the four cases. Perhaps most surprising is the fact that the crater diameter changes nonmonotonically as the drop height is increased. Since for a given projectile, the impact energy is proportional to h, the energy dependence of d_c is similarly nonmonotonic. This is very different from what is observed in the case of craters in granular materials, for which d_c shows a simple power-law dependence on impact energy [14,15,25].

Similar data from 19 different sphere-target combinations collapse onto a single curve when we plot d_c/d_b, the crater diameter scaled by the diameter of the sphere, against the impact Reynolds number Re, as in Fig. 5(a). The scaled crater diameter is constant for low Re, with an average value of 1.21 ± 0.05. Around Re = 10, d_c/d_b starts to decrease slightly, reaching a minimum value of slightly less than 1 at Re $\approx$ 40 before increasing again for larger Re. The Reynolds numbers corresponding to the craters shown in Figs. 2 and 3 are indicated by the arrows in Fig. 5(a). The scaled diameter data also collapse when plotted against the Mach number Ma, as shown in Fig. 5(b). In this case the minimum in crater diameter occurs at Ma $\approx$ 7. These two scalings imply different

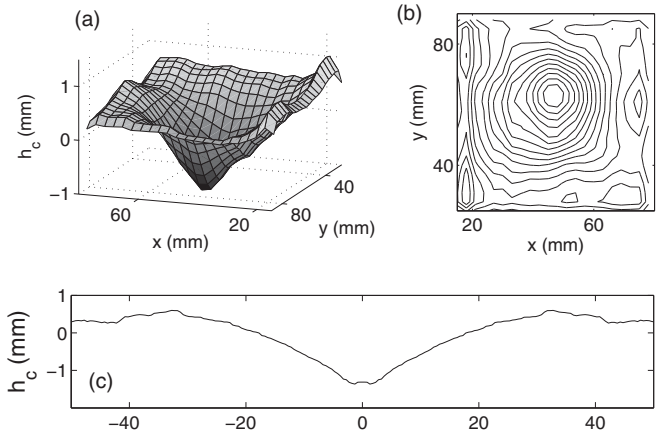

FIG. 3. (a) The three-dimensional surface of a crater in 0.5 wt % Carbopol formed by the impact of a 2.54 cm stainless steel sphere falling from a height $h = 0.050$ m. For this impact, Re = 24. The crater is roughly conical in shape with a small rim. (b) A contour plot of the same crater. (c) The azimuthally averaged crater profile. Note the different scales on the vertical and horizontal axes.

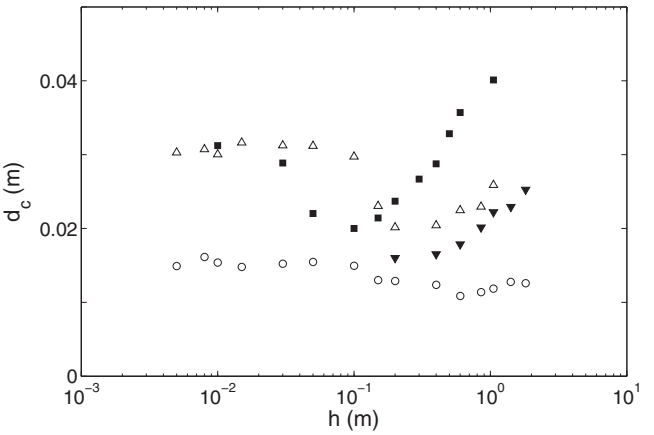

FIG. 4. Crater diameter d_c as a function of the release height h of the projectile. Data are shown for a steel sphere with $d_b = 1.27$ cm and $c = 2.2\%$ (circles), a stainless steel sphere with $d_b = 2.54$ cm and $c = 0.5\%$ (squares), an acetal sphere with $d_b = 2.54$ cm and $c = 2.2\%$ (upward-pointing triangles), and a steel sphere with $d_b = 1.91$ cm and $c = 1.2\%$ (downward-pointing triangles).

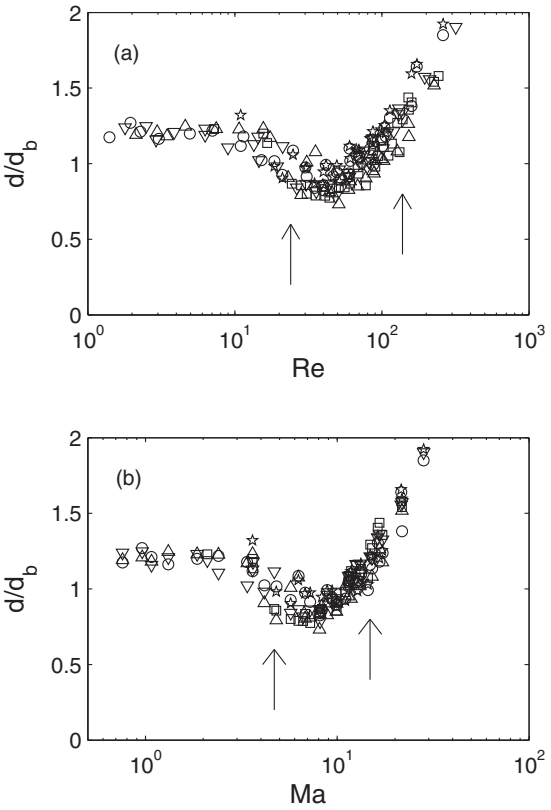

FIG. 5. (a) Scaled crater diameter plotted as a function of Re for chrome steel spheres with $d_b = 1.27$ (circles) and 1.91 cm (downward-pointing triangles), a tungsten carbide sphere, $d_b = 1.27$ cm (stars), an acetal sphere, $d_b = 2.54$ cm (upward-pointing triangles), and a stainless steel sphere, $d_b = 2.54$ cm (squares). Carbopol solutions with $c = 0.5$, 0.8, 1.2 and 2.2 wt % were used as targets. The arrows indicate the values of Re corresponding to the craters illustrated in Figs. 2 and 3. (b) The same data plotted as a function of Ma.

dependencies on fluid density and viscosity. Since all of our Carbopol dispersions had the same density, we were unable to test the density dependence, and we could not distinguish between the two on the basis of viscosity dependence; as seen in Fig. 5, the quality of the collapse is very similar in the two cases. The data do not collapse when plotted as a function of a scaled energy variable such as Fr.

C. Cavity closure

The depth z_v at which the entrained air cavity pinches off depends on both the impact velocity and the properties of the target material. Figure 6 shows z_v/d_b plotted as a function of Re. The data collapse fairly well onto a single curve and, as above, show a change in behavior at Re ≈ 10. For Re $\lesssim 10$, the pinch-off takes place approximately one sphere diameter below the surface—the mean value of z_v/d_b in this range is 1.16 ± 0.07—with perhaps a weak tendency to increase with increasing Re. In this low-Re regime, the time t_v at which the pinch-off occurs decreases as Re is increased, scaling approximately as $\mathrm{Re}^{-1/2}$. For Re $\gtrsim 20$, on the other hand, z_v/d_b increases approximately linearly with Re, while t_v becomes approximately constant. A similar collapse is found

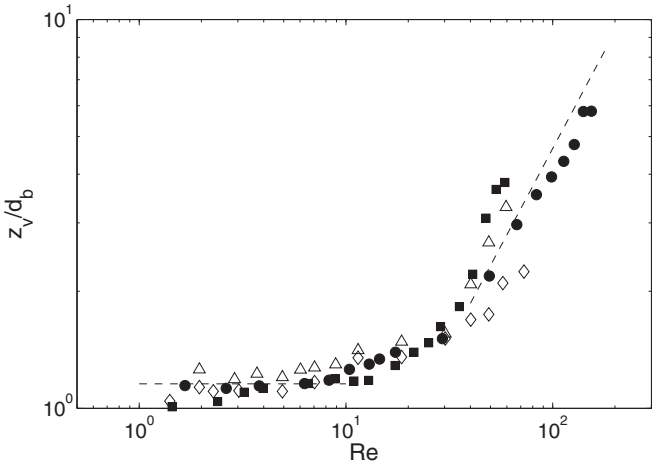

FIG. 6. The scaled cavity pinch-off depth z_v/d_b plotted as a function of Re for experiments with a chrome steel sphere, $d_b = 0.127$ m, $c = 1.0\%$ (squares); an aluminum oxide sphere, $d_b = 0.127$ m, $c = 0.5\%$ (circles); a chrome steel sphere, $d_b = 0.127$ m, $c = 2.2\%$ (diamonds); and a tungsten carbide sphere, $d_b = 0.127$ m, $c = 1.0\%$ (triangles). The dashed line drawn for Re $\leqslant 10$ indicates the mean value of z_v/d_b in this range, while the dashed line for Re > 40 is a fit to a linear relationship.

when z_v/d_b is plotted as a function of Ma. The same two regimes are also seen when these data are plotted as a function of Fr: z_v/d_b is approximately constant for low Fr, and increases roughly as Fr^2 for higher Fr. The data do not collapse onto a single curve at high Fr, however, and so behave differently from the numerical and analytical results found by Lohse *et al.* [16] in the context of granular materials.

We measured the radius r_v of the collapsing air cavity at its narrowest point as a function of time using our high-speed video camera recording at 1000 frames per second. Close to the pinch-off time, r_v shows a power-law dependence on the time to pinch-off [44]; i.e.,

$$r_v \propto (t_v - t)^{\alpha}. \tag{7}$$

The power-law exponents α determined from fits to the pinch-off data from experiments with a 0.127 cm chrome steel sphere in Carbopol with concentrations of 0.5 and 1.0 wt % are plotted as a function of Re in Fig. 7. Once again two regimes are observed: α is equal to 0.5 within the experimental scatter for Re $\gtrsim 40$, while α is higher (and the data are noisier) at lower Re, perhaps leveling off at a value close to one.

D. Jets

For sufficiently high impact velocities, the collapse of the entrained air cavity leads to the formation of a jet of Carbopol that shoots vertically upward. The analogous process also occurs in Newtonian [2,27] and viscoelastic fluids [6,7], as well as in loosely packed granular materials [13,15,16,29]. Figure 8 shows the formation and development of a small jet following the impact of a 2.54 cm acetal sphere into 0.8% Carbopol from a drop height of 0.595 m. The impact occurs in Fig. 8(a). In Fig. 8(b) the sphere has passed out of the field of view, leaving a long entrained air cavity behind it. There is a substantial "splash'—an upward deformation of the surface around the edge of the cavity—but by the time of Fig. 8(c),

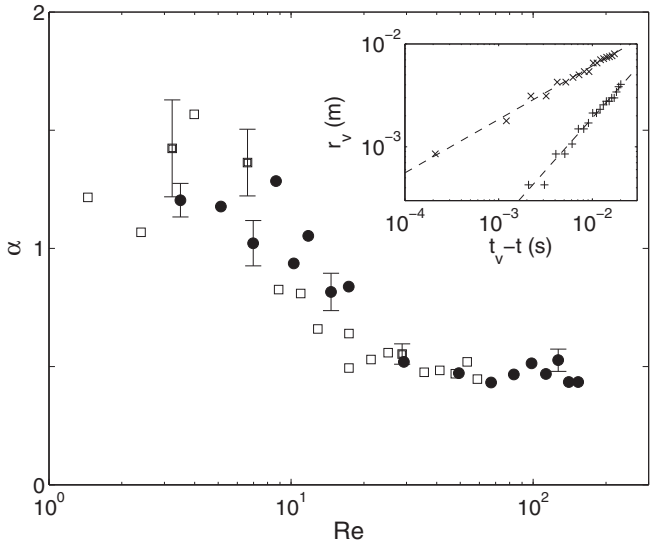

FIG. 7. The power-law exponent α determined by fitting Eq. (7) to data for the pinch-off of the entrained air cavity, plotted against Re. Typical uncertainties calculated by the fitting routine are shown for a few data points. Circles are for a Carbopol concentration of 0.5 wt % and squares for 1.0 wt %. In both cases the projectile was a 0.127 cm chrome steel sphere. The inset shows r_v, the minimum radius of the cavity, as a function of time to pinch-off for a concentration of 0.5 wt % and release height $h = 0.015$ m (+), and for 1.0 wt % and $h = 0.70$ m (×). The dashed lines are fits to Eq. (7), and give exponents $\alpha = 1.02 \pm 0.10$ and 0.53 ± 0.03, respectively.

this surface deformation has completely relaxed. The cavity has pinched off below the surface and its surface is moving upward. A small upward "bump" at the bottom of the cavity is barely visible in this image; it grows into the jet as time progresses. In Fig. 8(d) the bottom of the cavity is still below

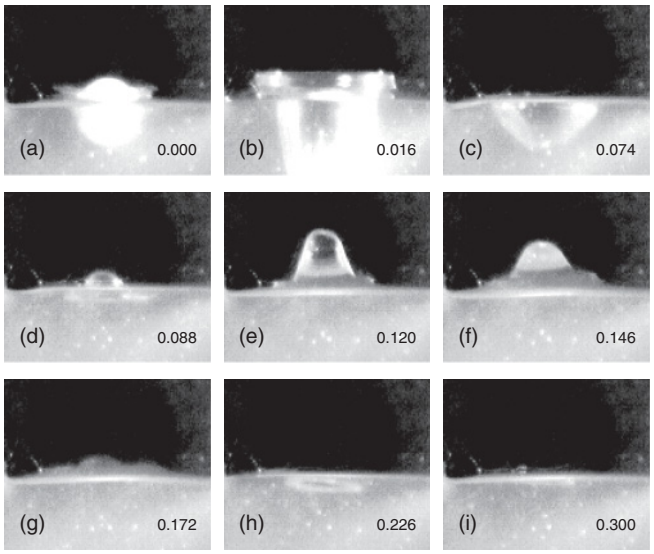

FIG. 8. The development of a small jet following the impact of a 2.54 cm acetal sphere into a 0.8% Carbopol dispersion. The release hight was 0.595 m and Re = 69. The relative time in seconds is indicated in the lower left corner of each image. The images are discussed in detail in the text.

the original surface level, but the jet has grown to the extent that its tip is visible above the surface. The jet reaches is maximum height around the time of Fig. 8(e). It has a tapered shape and rises out of a broad, low base with a diameter larger than that of the original cavity. In Fig. 8(f) the jet has started falling back down, while the level of the broader base is higher than in Fig. 8(e). At the time of Fig. 8(g), the jet has slumped almost back to the original surface level. In Fig. 8(h) the surface in the vicinity of the jet has sunk below the original Carbopol surface again, but it has rebounded slightly by Fig. 8(i), which is the final configuration.

In Fig. 9 we plot the maximum height of the jet h_j, measured relative to the original level of the free surface, as a function of the release height h for several combinations of spheres and Carbopol targets. At lower Carbopol concentrations, the upper portion of the jet often broke up into droplets; in these cases h_j is the maximum jet height before this instability occurred. In all cases the jet height increases linearly with h. The x intercept seen in the plots of Fig. 9 is partly a result of the fact that the jets form below the level of the original surface, around the depth of the air cavity's pinch-off. Consequently, jets did form for at least some release heights below the apparent threshold, but they did not rise above the original surface level and so could not be easily measured. Nonetheless our data do suggest that jets do not form for release heights below some threshold value. h_j is a strong function of the Carbopol concentration, with jets being much higher for targets with lower concentration [6,7]. This is illustrated by the inset to Fig. 9, in which the slopes of lines fit to data for $h_j(h)$ are plotted as a function of elastic modulus G for a single sphere and three different target concentrations. The fit shown in the inset indicates that

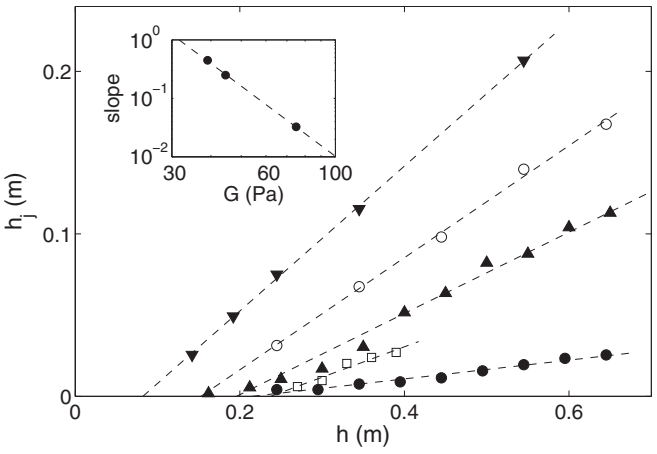

FIG. 9. The maximum jet height h_j, measured relative to the level of the original Carbopol surface, plotted as a function of the release height h of the impacting sphere. Open circles: chrome steel sphere, $d_b = 1.27$ cm, $c = 0.3$ wt %; squares: tungsten carbide sphere, $d_b = 1.27$ cm, $c = 0.5$ wt %; downward-pointing triangles: bronze sphere, $d_b = 1.91$ cm, $c = 0.3$ wt %; upward-pointing triangles: bronze sphere, $d_b = 1.91$ cm, $c = 0.5$ wt %; solid circles: acetal sphere, $d_b = 2.54$ cm, $c = 0.8$ wt %. The dashed lines are fits to the data. The inset is a logarithmic plot of the slopes obtained from such fits for runs with the bronze sphere with $d_b = 1.91$ cm, plotted against the elastic modulus G for three concentrations of Carbopol. The dashed line is a fit to the data and has a slope of -4.

the slope is proportional to G^{-4}. Larger spheres produced higher jets for a given release height, and h_j did not appear to depend on the density of the sphere—for a given Carbopol concentration, spheres of the same size but different material gave jets of the same height within the experimental scatter.

The jet height data do not appear to scale in any simple way with, for example, Re or Fr. Roughly speaking, jets do not form for Re $\lesssim 40$ (Ma $\lesssim 7$), or, in other words, the threshold for jet formation corresponds to the point at which the size of the crater starts to increase with Re. The fact that jet height is independent of the density of the projectile suggests that it is the speed of the impact, and not its energy, that determines the jet height. We were able to collapse our jet-height data by plotting h_j/d_b as a function of the dimensional quantity $(h - h_0)/G^4 d_b^{1/2}$. Here h_0 is the height threshold below which jet formation is not observed, and depends on both the projectile and the target material. The physical significance of this scaling, and in particular the strong dependence of h_j on the elastic modulus, is not understood.

IV. DISCUSSION

The dimensions of large-scale craters show a power-law scaling with the impact energy E. If all of the kinetic energy of the projectile is used to excavate the crater against the force of gravity, it is straightforward to show that the crater diameter d_c increases as $E^{1/4}$ [1]. In smaller craters (such as those formed by explosions), the energy required to overcome the strength of the target material dominates, in which case $d_c \sim E^{1/3}$ [1]. The diameter of low-energy impact craters formed in granular materials also shows a power-law dependence on E, with a power-law exponent close to 1/4 [12,14,15,25], although it has been demonstrated that only a very small fraction of the projectile's kinetic energy actually does work against gravity in granular impacts [25], with most of the energy being dissipated by friction and inelastic collisions among the grains.

As is clear from Fig. 4, the diameters of craters formed in our experiments on impact into a viscoplastic fluid behave very differently from what is observed in these other systems. In the present case, d_c varies nonmonotonically as the impact velocity is increased. In addition, the data from different runs do not collapse when plotted in terms of a scaled energy parameter such as the Froude number, but rather collapse when plotted as a function of the Reynolds number Re or the Mach number Ma. This indicates that the impact velocity, rather than the energy, is the important quantity in this process, and that the dimensions of the crater in this system depend on the nature of the flow within the target material, rather than on the energetics alone. This is in contrast with the simple energy scaling of crater dimensions observed in granular materials [12,14,15,25]. Since the simple scaling arguments referred to above assume that the crater shape is independent of the impact energy, the behavior we observe can also be taken as an indication that this assumption is violated in our experiments. This is clearly the case, as demonstrated by the crater profiles shown in Figs. 2 and 3.

For most of our runs, the Bingham number Bi < 1 at impact, indicating that the effect of the yield stress on the early dynamics is small compared to viscous effects. Elasticity is also expected to be negligible in the early stages of the process, although it clearly affects jet formation later on. When the impact velocity is small, i.e., when Re ~ 1, the target is yielded in the region around the projectile and the high shear stresses generated by the impact will largely be relieved by viscous dissipation. As Re increases, we expect the dynamics to become governed more by inertia, with viscosity becoming relatively unimportant. At high values of Ma, the impacts are supersonic with respect to shear waves in the target [42], meaning that the transmission of shear stresses is slow compared to the motion of the projectile. Far enough from the projectile, the stress in the Carbopol is always less than its yield stress and it behaves as an elastic solid. The flow in the Carbopol target changes strongly with time over the course of an experiment, and at the later stages elasticity and yield stress are expected to become more important as the shear stress in the Carbopol decreases toward τ_c. Indeed, it is the yield stress that results in a crater remaining in the material once all flow has stopped. It has recently been shown that in Newtonian fluids, air entrainment only occurs for an impact speed higher than a critical value that depends on the wetting properties of the fluid on the surface of the projectile [57]. It is essentially impossible to determine the contact angle of Carbopol on a solid surface because of its yield stress, but we note that some air entrainment was observed in all of our experiments.

We observe two distinct regimes in both the cavity pinch-off dynamics and the resulting crater diameter. At lower values of the impact Reynolds number, the crater diameter is constant and only slightly larger than the diameter of the projectile. In this viscous regime, as the sphere penetrates the Carbopol, its passage produces stresses which exceed the yield stress in a region of radial extent of order d_b around the sphere [45–48,51]. The fluid in this region is thus able to flow, while further from the sphere the Carbopol remains solid. Incompressibility forces the displaced Carbopol to form a backflow around the falling sphere, and lateral pressure due to a combination of gravity and perhaps elasticity forces it into the air cavity left behind the sphere. This leads to a pinch-off of the air cavity at a depth that is again slightly larger than the size of the sphere and independent of the impact speed. The upper part of the cavity relaxes upward towards the level of the original surface due to a combination of flow and the relaxation of elastic deformation. If the Carbopol remained fluid, the cavity would eventually end up with a flat free surface. As the stress within the material decreases below the yield stress, however, a roughly conical crater is left in the surface of the material. This crater is the fossil of the part of the air cavity above the pinch-off point. Its size is determined by the diameter of the original cavity, which in turn is determined only by the projectile size. This explains the observed constancy of d_c/d_b in this regime. As Re increases and inertial effects become more dominant, the crater diameter decreases slightly. The backflow around the falling sphere becomes stronger and the pressure driving the collapse of the entrained air cavity higher. As a result, the cavity collapses more energetically and relaxes further toward the surface, leaving a smaller crater at the end of the process.

For even higher impact speeds, in contrast, d_c/d_b increases with speed. The entrained air cavity is also much longer in this regime, and the pinch-off of the cavity occurs at larger depths. In this regime, the pinch-off is sufficiently energetic

that it induces the formation of a jet, and the relaxation of the cavity after pinch-off is underdamped—the cavity recoils up past the original surface level, then subsides again, as shown in Fig. 8. In the process, it produces disturbances on the material surface that are significantly larger in extent than the original cavity. In this regime, the morphology of the crater reflects the jet-formation process, with the diameter of the crater being determined by the extent of the surface disturbances and the central peak being the remains of the jet itself.

The air cavity entrained by a projectile impacting a fluid surface, and in particular its collapse and pinch-off, has been studied in several contexts [3–5,16,20,26–28,44,50]. In the simplest case, the collapse of the cavity is driven solely by hydrostatic pressure. The effect of interstitial air has been shown to be important in granular materials [20]. The fluid at the top of the cavity starts to collapse inward first, but the driving pressure there is low. The pressure is higher at greater depths, but the collapse starts later. These competing effects result in there being a particular depth at which the collapse happens first, which has been shown to scale as $\mathrm{Fr}^{1/3}$ [16]. The pinch-off has been described in both Newtonian fluids and granular materials by a cylindrical version of the Rayleigh-Plesset equation for the radius of the cavity [16,44,53]. This equation has solutions of the form $r \sim (t_v - t)^{\alpha}$, with $\alpha = 1/2$ if the collapse is dominated by inertial effects, and $\alpha = 1$ if viscosity dominates. A transition between these two regimes has been observed in the pinch-off of bubbles [44], while deviations from the $\alpha = 1/2$ behavior were investigated in Ref. [5].

In general terms, the formation and pinch-off of the entrained air cavity in Carbopol is similar to the analogous phenomena in Newtonian fluids and granular materials, and the scaling of the pinch-off with time appears to be quantitatively consistent with that observed in other fluids. As shown in Fig. 7, we observe $r \sim (t_v - t)^{1/2}$ at high Re, where inertial effects dominate. We also observe a transition to a regime with a higher power-law exponent at lower Re as viscous effects become more important, as in Ref. [44], and, although our data are somewhat scattered at low Re, they are consistent with the power-law exponent α being equal to one in that regime. This level of agreement suggests that the rheology of Carbopol does not have a major effect on the pinch-off dynamics in our experiments. This is not entirely surprising, since for most of the process we expect the effects of both yield stress and elasticity on the fluid flow to be small. On the other hand, the depth of the cavity pinch-off does not scale with Fr in the manner calculated by Lohse *et al.* [16], suggesting that forces other than hydrostatic pressure are involved at some level. This may reflect a contribution to the pressure due to unyielded material further from the axis of impact acting to confine the backflow of the Carbopol displaced by the sphere.

Jets similar to those we observe in our experiments are well known in simple fluids [2,9,27,52] and have also been studied in viscoelastic fluids [6,7] and granular materials [13, 16,20]. The process leading to the formation of jets in our experiments is qualitatively similar to that in other materials. Material flowing radially inward during the collapse of the air cavity is deflected upward (or downward) by the sudden increase in pressure that occurs when the cavity closes off [13]. The height of jets in granular materials has been observed to increase roughly linearly with the release height of the impacting sphere, at least for small drop heights [13,16,20], in agreement with the present results. On the other hand, we observe an apparent threshold release height below which jets do not form, while there is no evidence for such a threshold in other target materials. In fact, relatively large jets have been observed with a release height of zero (i.e., with the bottom of the sphere touching the target surface) in the very loosely packed granular materials studied in Ref. [16].

Cheny and Walters have studied the effects of elasticity on jets formed when a spherical projectile falls into polymer solutions [6,7]. They found that the jet height decreased dramatically as the polymer concentration increased, and attributed this to the extensional viscosity of the solutions. In addition to being elastic, our materials have a yield stress and are strongly shear thinning. Carbopol gels consist of strongly interacting, swollen polymer microgel particles, and little is known about their extensional rheology. As a result, while we also observe a strong decrease of the height of the jet with an increase in polymer concentration, it is not yet clear whether the physical origin of this decrease is the same as that found in Refs. [6,7] or if it is related to the rheology of the Carbopol in other ways.

Models of the collapse of a transient impact crater in a Bingham fluid [described by Eq. (1) with $n = 1$] have been introduced to explain the formation of a central peak in complex planetary craters via underdamped oscillations of the fluidized material in the crater [31,32]. This is exactly analogous to the process of jet formation and collapse illustrated in Fig. 8. The morphologies of craters produced by hypervelocity (i.e., km/s) impacts into clay slurries with yield stresses ranging from a few to a few thousand Pa have been compared to those of planetary craters [30,32,33], and it has been recognized that the yield stress is responsible for the crater remaining once the actual flow has died out. As in our Carbopol experiments, the crater is the formed by the surface deformation that remains when the stress in the target material drops below τ_c. Based on these similarities, our experiments may be viewed as a simple, phenomenological model of the geophysical impact cratering process. There are, however, significant differences between our results and the expected behavior of large-scale impacts, the most obvious being the nonmonotonic dependence of the scaled crater diameter on Re and the absence of the expected energy scaling. We estimate the impact Reynolds number in the clay-slurry experiments of Refs. [30,32,33] to be at least several thousand, significantly higher than in ours. Re in planetary impacts is likely very much larger than that. This will undoubtedly change the details of the subsurface flow. In addition, notion of air entrainment in a high-speed meteor impact seems questionable, since in that case the impactor is much smaller than the size of the final crater, and is essentially completely vaporized by the impact. It would be interesting to extend our experiments to higher Re by, for example, tuning the fluid properties, to see whether the crater diameter eventually starts to scale with energy.

V. CONCLUSIONS

We have studied several aspects of the impact of a spherical projectile into Carbopol, a model yield-stress fluid. We find

that our results generally collapse when plotted as a function of the Reynolds number or the Mach number, suggesting that the behavior following the impact depends on the velocity of the projectile and the nature of the subsequent subsurface flow rather than on the impact energy. At low Re, viscous effects are significant. In this regime, the pinch-off of the air cavity entrained by the sphere decreases linearly with time and the diameter of the crater remaining after the Carbopol has returned to its solid state is constant and only slightly bigger than the diameter of the sphere. At high Re, the cavity radius decreases as $(t - t_v)^{1/2}$ and the cavity collapse results in the formation of vertically directed jets. The jet height increases linearly with the release height of the sphere, but with a threshold below which no jets are observed, and depends strongly on the elastic modulus of the Carbopol dispersion. In this high-Re regime, the morphology and size of the crater are determined by the flow of materials during the development and collapse of the jet. The final crater profile in all cases reflects the state of the fluid when the stress decreases below the yield stress and the material becomes solid.

ACKNOWLEDGMENT

This research was supported by NSERC of Canada.

[1] H. J. Melosh, *Impact Cratering: A Geologic Process* (Oxford University Press, New York, 1989).
[2] M. A. Worthington, *A Study of Splashes* (Longman, Green, London, 1908).
[3] J. W. Glasheen and T. A. McMahon, Phys. Fluids **8**, 2078 (1996).
[4] S. Gaudet, Phys. Fluids **10**, 2489 (1998).
[5] R. Bergmann, D. van der Meer, M. Stijnman, M. Sandtke, A. Prosperetti, and D. Lohse, Phys. Rev. Lett. **96**, 154505 (2006).
[6] J. M. Cheny and K. Walters, J. Non-Newtonian Fluid Mech. **67**, 125 (1996).
[7] J.-M. Cheny and K. Walters, J. Non-Newtonian Fluid Mech. **86**, 185 (1999).
[8] A. Bisighini, G. E. Cossali, C. Tropea, and I. V. Roisman, Phys. Rev. E **82**, 036319 (2010).
[9] A. I. Fedorchenko and A. B. Wang, Phys. Fluids **16**, 1349 (2004).
[10] A. L. Yarin, Annu. Rev. Fluid Mech. **38**, 159 (2006).
[11] A. Prosperetti and H. N. Oguz, Annu. Rev. Fluid Mech. **25**, 577 (1993).
[12] J. C. Amato and R. E. Williams, Am. J. Phys. **66**, 141 (1988).
[13] S. T. Thoroddsen and A. Q. Shen, Phys. Fluids **13**, 4 (2001).
[14] J. S. Uehara, M. A. Ambroso, R. P. Ojha, and D. J. Durian, Phys. Rev. Lett. **90**, 194301 (2003).
[15] A. M. Walsh, K. E. Holloway, P. Habdas, and J. R. de Bruyn, Phys. Rev. Lett. **91**, 104301 (2003).
[16] D. Lohse, R. Bergmann, R. Mikkelsen, C. Zeilstra, D. van der Meer, M. Versluis, K. van der Weele, M. van der Hoef, and H. Kuipers, Phys. Rev. Lett. **93**, 198003 (2004).
[17] K. A. Newhall and D. J. Durian, Phys. Rev. E **68**, 060301 (2003).
[18] J. R. de Bruyn and A. M. Walsh, Can. J. Phys. **82**, 439 (2004).
[19] M. P. Ciamarra, A. H. Lara, A. T. Lee, D. I. Goldman, I. Vishik, and H. L. Swinney, Phys. Rev. Lett. **92**, 194301 (2004).
[20] J. R. Royer, E. I. Corwin, A. Flior, M.-L. Cordero, M. L. Rivers, P. J. Eng, and H. M. Jaeger, Nature Phys. **1**, 164 (2005).
[21] M. A. Ambroso, C. R. Santore, A. R. Abate, and D. J. Durian, Phys. Rev. E **71**, 051305 (2005).
[22] M. A. Ambroso, R. D. Kamien, and D. J. Durian, Phys. Rev. E **72**, 041305 (2005).
[23] L. S. Tsimring and D. Volfson, in *Powders and Grains 2005*, edited by H. J. Herrmann, R. Garcia-Rojo, and S. McNamara (Balkema, Rotterdam, 2005), Vol. 2, p. 1215.
[24] H. Katsuragi and D. J. Durian, Nature Phys. **3**, 420 (2007).
[25] S. J. de Vet and J. R. de Bruyn, Phys. Rev. E **76**, 041306 (2007).
[26] S. Gekle, A. van der Bos, R. Bergmann, D. van der Meer, and D. Lohse, Phys. Rev. Lett. **100**, 084502 (2008).
[27] S. Gekle, J. M. Gordillo, D. van der Meer, and D. Lohse, Phys. Rev. Lett. **102**, 034502 (2009).
[28] S. Gekle, I. R. Peters, J. M. Gordillo, D. van der Meer, and D. Lohse, Phys. Rev. Lett. **104**, 024501 (2010).
[29] J. O. Marston, J. P. K. Seville, Y.-V. Cheun, A. Ingram, S. P. Decent, and M. J. H. Simmons, Phys. Fluids **20**, 023301 (2008).
[30] R. Greeley, J. Fink, D. E. Gault, D. B. Snyder, J. E. Guest, and P. H. Shultz, Proc. Lunar Planet. Sci. Conf. **11**, 2075 (1980).
[31] H. J. Melosh, Proc. Lunar Planet. Sci. Conf. **12**, 702 (1981).
[32] J. H. Fink, R. Greeley, and D. E. Gault, Proc. Lunar Planet. Sci. **12B**, 1649 (1981).
[33] D. E. Gault and R. Greeley, Icarus **34**, 486 (1978).
[34] Lubrizol Technical Data Sheet No. 216 (unpublished).
[35] R. J. Ketz Jr., R. K. Prud'homme, and W. W. Graessley, Rheol. Acta **27**, 531 (1988).
[36] I. Gutowski, D. Lee, J. R. de Bruyn, and B. Frisken (unpublished).
[37] H. Tabuteau, P. Coussot, and J. R. de Bruyn, J. Rheol. **51**, 125 (2007).
[38] F. K. Oppong, L. Rubatat, B. J. Frisken, A. E. Bailey, and J. R. de Bruyn, Phys. Rev. E **73**, 041405 (2006).
[39] F. K. Oppong, and J. R. de Bruyn, J. Non-Newtonian Fluid Mech. **142**, 104 (2007).
[40] J.-M. Piau, J. Non-Newtonian Fluid Mech. **144**, 1 (2007).
[41] V. Bertola, J. Phys. Condens. Matter **21**, 035107 (2009).
[42] H. Tabuteau, D. Sikorski, and J. R. de Bruyn, Phys. Rev. E **75**, 012201 (2007).
[43] B. Akers and A. Belmote, J. Non-Newtonian Fluid Mech. **135**, 97 (2006).
[44] J. C. Burton, R. Waldrep, and P. Taborek, Phys. Rev. Lett. **94**, 184502 (2005).
[45] A. Beris, J. A. Tsamopoulos, R. C. Armstrong, and R. A. Brown, J. Fluid Mech. **158**, 245 (1985).
[46] D. D. Attapattu, R. P. Chhabra, and P. H. T. Uhlherr, J. Non-Newtonian Fluid Mech. **38**, 31 (1990).
[47] D. Deglo de Besses, A. Magnin, and P. Jay, AIChE J. **50**, 2627 (2004).
[48] J. R. de Bruyn, Rheol. Acta **44**, 150 (2004).
[49] D. Sikorski, H. Tabuteau, and J. R. de Bruyn, J. Non-Newtonian Fluid Mech. **159**, 10 (2009).

[50] M. Lee, R. G. Longoria, and D. E. Wilson, Phys. Fluids **9**, 540 (1997).
[51] J. Blackery and E. Mitsoulis, J. Non-Newtonian Fluid Mech. **70**, 59 (1997).
[52] J. E. Hogrefe, N. L. Pelley, C. L. Goodridge, W. T. Shi, H. G. E. Hentschel, and D. P. Lathrop, Physica D **123**, 183 (1998).
[53] H. N. Oguz and A. Prosperetti, J. Fluid Mech. **257**, 111 (1993).
[54] J. M. Gordillo, A. Sevilla, J. Rodríguez-Rodríguez, and C. Martínez-Bazán, Phys. Rev. Lett. **95**, 194501 (2005).
[55] J. Eggers, M. A. Fontelos, D. Leppinen, and J. H. Snoeijer, Phys. Rev. Lett. **98**, 094502 (2007).
[56] S. T. Thoroddsen, T. G. Etoh, and K. Takehara, Phys. Fluids **19**, 042101 (2007).
[57] C. Duez, C. Ybert, C. Clanet, and L. Bocquet, Nature Phys. **3**, 180 (2007).